A chordate species lacking *Nodal* utilizes calcium oscillation and *Bmp* for left–right patterning

Takeshi A. Onuma[a,1], Momoko Hayashi[a], Fuki Gyoja[b], Kanae Kishi[a], Kai Wang[a], and Hiroki Nishida[a]

[a]Department of Biological Sciences, Graduate School of Science, Osaka University, 560-0043 Toyonaka, Osaka, Japan; and [b]Marine Genomics Unit, Okinawa Institute of Science and Technology Graduate University, 904-0495 Onna, Okinawa, Japan

Edited by Edward M. De Robertis, David Geffen School of Medicine, University of California, Los Angeles, CA, and approved December 20, 2019 (received for review September 27, 2019)

Larvaceans are chordates with a tadpole-like morphology. In contrast to most chordates of which early embryonic morphology is bilaterally symmetric and the left–right (L–R) axis is specified by the Nodal pathway later on, invariant L–R asymmetry emerges in four-cell embryos of larvaceans. The asymmetric cell arrangements exist through development of the tailbud. The tail thus twists 90° in a counterclockwise direction relative to the trunk, and the tail nerve cord localizes on the left side. Here, we demonstrate that larvacean embryos have nonconventional L–R asymmetries: 1) L- and R-cells of the two-cell embryo had remarkably asymmetric cell fates; 2) Ca^{2+} oscillation occurred through embryogenesis; 3) *Nodal*, an evolutionarily conserved left-determining gene, was absent in the genome; and 4) bone morphogenetic protein gene (*Bmp*) homolog *Bmp.a* showed right-sided expression in the tailbud and larvae. We also showed that Ca^{2+} oscillation is required for *Bmp.a* expression, and that BMP signaling suppresses ectopic expression of neural genes. These results indicate that there is a chordate species lacking *Nodal* that utilizes Ca^{2+} oscillation and *Bmp.a* for embryonic L–R patterning. The right-side *Bmp.a* expression may have arisen via cooption of conventional BMP signaling in order to restrict neural gene expression on the left side.

larvacean | left–right asymmetry | $Ca2^{+}$ oscillation | Bmp | chordate

More than a century ago, it was found that embryos of the larvacean *Oikopleura dioica* show exceptional left–right (L–R) asymmetry as early as the four-cell embryo stage (1–3). Larvaceans are members of the tunicate subphylum, which includes the closest relatives to vertebrates. During embryogenesis of *O. dioica*, the first and second embryonic cleavages take place in L–R and anterior–posterior directions, respectively, as with most ascidian species. In the four-cell embryo, however, anterior-left and posterior-right blastomeres are formed slightly closer to the vegetal pole, contacting each other at the vegetal side (Fig. 1). The asymmetric cell contacts are stable during the cleavage stages, forming an intricate median plane (2, 3). After gastrulation, the tail of the tadpole larvae gradually rotates 90° in a counterclockwise direction relative to the trunk (4). Consequently, the nerve cord is located on the left side, not the dorsal side, of the notochord. The twisted positioning of the nerve cord is already visible in the prehatching tailbud (Fig. 1 *H* and *J*), and is clearly evident in the adult body (5–7). In the present study, we focused on this novel L–R patterning process of a chordate species.

In the early embryos of most animals, the morphology is bilaterally symmetric; later in development, a symmetry break occurs that leads to L–R patterning (8–10). In contrast to dorsal–ventral (D–V) patterning, in which transforming growth factor-β (TGF-β) family proteins, including bone morphogenesis proteins (BMPs), are known to form conserved pathways for neural formation (11–13), L–R symmetry breaking shows striking diversity, and different models have been proposed in a variety of animal species. These models include cilia-driven fluid flow (14–16), intracellular ion flux (17–19), cilia-driven calcium oscillation (20, 21), cellular rearrangement through cytoskeletal polarity (22–25), directional cell migration (26), and directional rotation of the neurula by ciliary movement (27, 28). These are considered to be biological cues that induce the left-sided expression of *Nodal*, a member of the TGF-β family, leading to the L–R asymmetry of Deuterostomia (e.g., vertebrates) and Lophotrochozoa (e.g., pond snails). However, these mechanisms are not universal. For example, motile cilia are not associated with L–R patterning in the pond snail (29, 30), and *Nodal* is lost in Ecdysozoa (e.g., nematodes and flies). This diversity of symmetry-breaking mechanisms suggests that there may be organisms with novel strategies for L–R patterning.

O. dioica is a planktonic tunicate that retains a notochord and tadpole-like morphology throughout its life. Its notable features include rapid development, with complete morphogenesis occurring within 10 h postfertilization (hpf) at 19 to 20 °C; a low number of cells (~3,500 in functional juveniles); and a transparent body (2, 3). Its embryonic cell lineages and fate map have been well described (3, 4, 31). Thus, *O. dioica* could serve as a valuable system to monitor chordate development at the single-cell resolution by live imaging (32, 33). Furthermore, the larvacean has a small and differently arranged genome compared to those in other nonparasitic metazoans (34, 35), and is known as a "successful gene-loser" that lacks many evolutionarily conserved genes such as those for retinoic acid signaling (36) and nonhomologous DNA end-joining (37). In addition, the *Oikopleura* embryo does

Significance

There is a chordate species with a nonconventional strategy for left–right (L–R) patterning. L–R asymmetry emerges in the four-cell embryos of the larvacean *Oikopleura dioica*. The asymmetric cell arrangements exist throughout development, and the nerve cord is located on the left, not dorsal, side of tadpole-shaped larvae. Here, we reveal that *O. dioica* lacks Nodal in the genome, but utilizes Ca^{2+} oscillation and right-sided Bmp expression for embryonic L–R patterning. It is well established that the dorsal–ventral (D–V) axis is inverted 180° between insects and vertebrates in correlation with Bmp expression. Our data serve as an example that the D–V axis and Bmp expression can induce a 90° rotation with L–R patterning.

Author contributions: T.A.O. and H.N. designed research; T.A.O., M.H., and K.K. performed research; T.A.O., F.G., and K.W. performed sequence analyses; T.A.O., M.H., and K.K. contributed new reagents/analytic tools; T.A.O., M.H., F.G., K.K., and K.W. analyzed data; and T.A.O. and H.N. wrote the paper.

The authors declare no competing interest.

This article is a PNAS Direct Submission.

Published under the PNAS license.

Data deposition: Primer pairs were designed to amplify cDNA fragments; their sequences and the identifiers for genes used in the present study are shown in *SI Appendix*, Table S1. Sequences of the ANISEED transcript models and Oikobase transcripts can be accessed from the following URLs: ANISEED: https://www.aniseed.cnrs.fr/; OikoBase: http://oikoarrays.biology.uiowa.edu/Oiko/.

[1]To whom correspondence may be addressed. Email: takeo@bio.sci.osaka-u.ac.jp.

This article contains supporting information online at https://www.pnas.org/lookup/suppl/doi:10.1073/pnas.1916858117/-/DCSupplemental.

First published February 6, 2020.

Downloaded at Palestinian Territory, occupied on December 7, 2021

www.manaraa.com

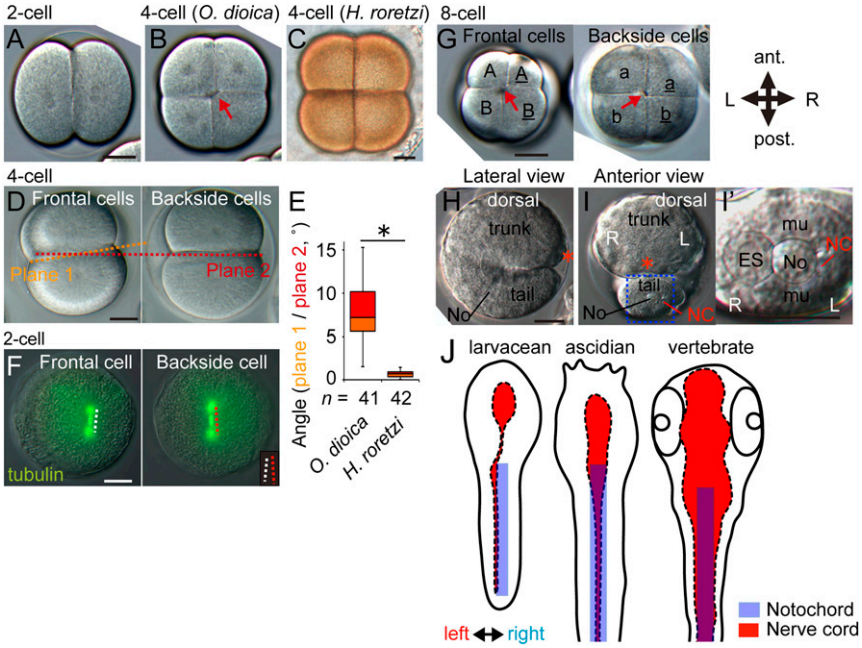

Fig. 1. L–R asymmetry consistently emerges at the four-cell embryo stage of larvaceans. (*A*–*C*) Vegetal view of the two-cell embryo (*A*) and four-cell embryo (*B*) of the larvacean *O. dioica*, and four-cell embryo of the ascidian *H. roretzi* (*C*). Red arrow indicates the asymmetric contact point of the anterior-left and posterior-right blastomeres. Note that the orientation of embryos in *A* and *B* is the same as in *G*. (*D*) Side views of the four-cell embryo. Cleavage planes for the frontal and backside cells are labeled as plane 1 (dashed orange line) and plane 2 (dashed red line), respectively. The orientation of embryos was not determined. (*E*) Angle between plane 1 and plane 2 (*$P < 0.01$, Student's *t* test). (*F*) Immunostaining of tubulin. Mitotic apparatus is not parallel between the L- and R-cells of the two-cell embryo. The spindle orientations in the frontal and backside cells are marked with white and red dashed lines, respectively. *Right Insets* represent the angle between the white and red lines. (*G*) Vegetal view of the eight-cell embryo. Lowercase and capital letters indicate blastomeres at the animal and vegetal hemispheres, respectively. Red arrows depict the asymmetric contact points of the blastomeres. Right blastomeres are distinguished from left ones by underlined letters. (*H* and *I*) Prehatching tailbud embryos from a lateral (*H*) and anterior (*I*) view. In the tail, the nerve cord (NC) was located on the left side of the notochord (No). Red asterisks indicate the anterior tip. The image to the right of *I* is an enlarged view (*I'*). ES, endodermal strand; mu, muscle. (Scale bars, 20 μm and 50 μm for *O. dioica* and *H. roretzi*, respectively.) (*J*) The nerve cord is located on the left side of the tail. Schematic illustration of the nervous system (red) and notochord (blue) in the tadpole larva of larvacean, ascidian, and vertebrate (zebrafish). Dorsal views.

not have cilia that can be used for symmetry breaking. These features provide an opportunity to explore how L–R patterning mechanisms can diverge in chordates to conserve the tadpole-like shape.

In the present study, we aimed to determine how embryonic L–R asymmetry affects the L–R asymmetry patterning of larvacean larvae.

Results

L–R Asymmetry in Blastomere Arrangement. We first confirmed previous reports that the first sign of L–R asymmetry is visible in the four-cell embryo (1, 2). To determine the side of observation, images were successively taken from the two- to eight-cell stage, of which left and right sides can be distinguished by cell size and topological arrangement (Fig. 1*G*). The morphology of the two-cell embryo is bilateral (Fig. 1*A*), as in all ascidians and most vertebrates. Hereafter, we designated the blastomeres as the left (L-) and right (R-) cell. The second and third cleavages occurred along the anterior–posterior and animal–vegetal axes, respectively (Fig. 1 *B*, *D*, and *G*). In the four-cell embryo, the anterior-left and posterior-right blastomeres always formed slightly closer to the vegetal pole, resulting in contact at the vegetal pole (Fig. 1*B*, red arrow). On the other hand, the anterior-right and posterior-left blastomeres made contact at the animal pole. Thus, the second cleavage planes that bisect the L- and R-cells were not precisely parallel (Fig. 1*D*). This was not the case in the four-cell embryos of the ascidian *Halocynthia roretzi* (Fig. 1*C*). To statistically validate these observations, the angles between the second cleavage planes on both sides were measured (Fig. 1*E*). The angle in the *O. dioica* embryo was 7.2° on average, and significantly larger than that of *H. roretzi* (1.8° on average). The blastomeres were thus shifted in the same direction in all embryos, although the angle varied among embryos. These results confirmed that the *O. dioica* embryo already shows L–R asymmetry as early as the four-cell stage.

The L–R asymmetry of the four-cell embryos appeared to originate with an event in the L- and R-cells of the two-cell embryo. Time-lapse observation showed that the cell division planes of the L- and R-cells were not parallel to each other (Movie S1). Accordingly, our visualization of tubulin indicated that the mitotic apparatus in the L- and R-cells were not parallel (Fig. 1*F*). This misalignment was observed in all embryos examined ($n = 23$), suggesting that some L–R asymmetric processes occurred during the two-cell stage.

The asymmetric contact of blastomeres was maintained after the eight-cell stage (Fig. 1*G*, red arrows). The median plane is known to gradually tilt along the anterior–posterior axis during embryogenesis (2–4). In our observations, the tail expectedly showed an ~90° counterclockwise twist relative to the trunk of the tailbud (Fig. 1 *H* and *I*) and in tadpole larvae (Fig. 1*J*), although the causal relationship between the L–R asymmetry of the blastomeres and the tail twist remains unknown. This twist makes defining the D–V and L–R axes complicated. However, when the D–V axis is set in reference to the trunk, the tail nerve cord is located on the left, not dorsal, side of the notochord (Fig. 1 *I'* and *J*). This L–R asymmetry was also evident when *tubulin 1A* was expressed in the nerve cord, as observed through in situ hybridization (38, 39). The nerve cord has been shown to include descendants from both L- and R-cells, although it is present on the left side of the tail (4).

Downloaded at Palestinian Territory, occupied on December 7, 2021

www.manaraa.com

Collectively, we hypothesized that early embryonic L–R asymmetry could be at the root of the morphological L–R asymmetry in the tadpoles. Next, we aimed to characterize the differences between the L- and R-cells at the two-cell stage, as well as those between their descendants throughout embryogenesis.

L- and R-Cells of the Two-Cell Embryo Show Distinct Cell Fates. First, we investigated the fates of the L- and R-cells in the two-cell embryo. In ascidians and *Xenopus*, cells descending from the L- or R-cell primarily form the bilateral halves of larval and adult bodies (40–42). In contrast, our recent study of the trunk epidermis of *O. dioica* showed that the boundaries of L- and R-descendants were largely disparate from the midline (33). While the cell lineages and the 3D positions of nuclei have been well described before the hatching period (tailbud stage, around 2.5 hpf) (4), it is unclear whether the L- and R-cells have similar cell fates in fully formed juveniles that have undergone complete cell differentiation and organ formation. To investigate this, a cell-labeling experiment was carried out. As shown in Fig. 2*A*, the L- or R-cell from the two-cell embryos expressing the photoconvertible nls-Kaede protein was illuminated with UV light to change its color from green to red. Red-colored nls-Kaede proteins were inherited in the descendant cells (Fig. 2*A*). *Z*-stack images of red-colored nuclei at 8 to 10 hpf allowed us to investigate the distributions of descendant nuclei in functional juveniles at a single-cell resolution (Movie S2). First, we compared our results with those of previously described muscle and notochord cells in tailbud embryos (Fig. 2*C* and *SI Appendix*, Fig. S1*D*). Our results were in perfect agreement with those previous findings (4). Our analysis further clarified the origins of the 9th and 10th pairs of muscle cells in the tip of the tail and the tip cell of the notochord, which are generated after hatching and thus were not clarified in the previous study. These cells were found to be descendants of the R-cell (Fig. 2 *B* and *C* and *SI Appendix*, Fig. S1 *A–D*).

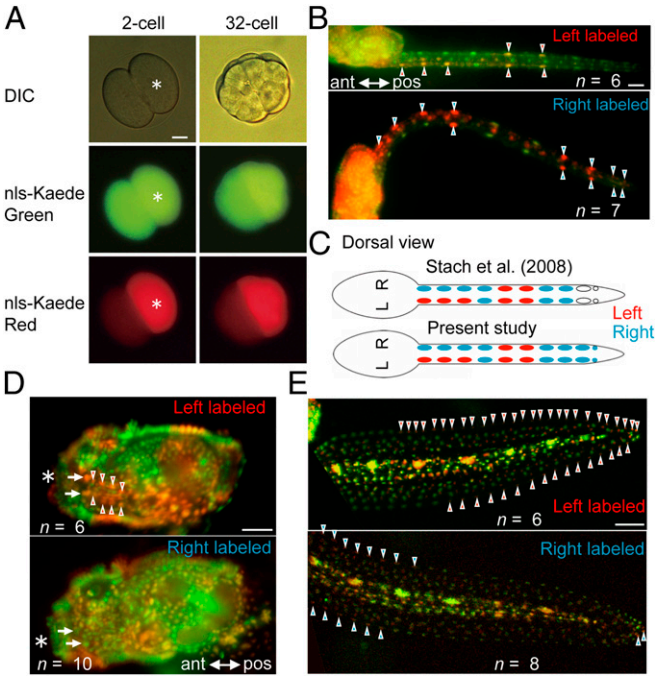

Fig. 2. L- and R-cells have asymmetric cell fates. (*A*) The L- or R- cell of the two-cell embryo was illuminated by UV light to convert the nls-Kaede green fluorescent dye to red (asterisks). (*B*) Muscle cells. Red and blue arrowheads represent descendants of the L- and R-cell, respectively. (*C*) Comparison of muscle cell fates with that of a previous report (*Upper*) (4) and the present study (*Lower*). Both were in good agreement. The 9th and 10th pairs of muscle cells at the tip of the tail were not described in the previous study. (*D*) Ventro-lateral view of four giant endostyle cells, aligned in each bilateral line (arrows). Asterisk indicates the mouth. (*E*) Edge cells of the tail fin epidermis. Red and blue arrowheads represent descendants of the L- and R-cell, respectively. (Scale bars, 20 μm.)

Descendant cells of the L- and R-cells were distributed asymmetrically throughout the organism, even in most morphologically symmetric organs (Fig. 2 and *SI Appendix*, Fig. S1 *E–G*). A representative example is the endostyle, a U-shaped symmetric organ on the ventral side of the trunk (7, 43). Unexpectedly, descendants of the L-cell occupied all bilateral giant cells (four cells on each side) in the endostyle (Fig. 2*D*). No descendants of the R-cell were found. Similarly, both oral glands, a symmetric pair of cells in the vicinity of the mouth, were L-descendants (*SI Appendix*, Fig. S1*E*). In contrast, the subchordal cells, a pair of cells in the ventral tail, were R-descendants (*SI Appendix*, Fig. S1*F*). The oral gland and subchordal cells have been proposed to share an ontogenic origin, because only larvacean species with an oral gland have subchordal cells (44). However, our results suggest that these two cells had a different origin.

Thus, the cell boundary between the L- and R-descendants is complex and is not split along the midline. This was also observed in the tail epidermis (Fig. 2*E* and *SI Appendix*, Fig. S1*G*). The tail epidermis consists of an epithelial sheet monolayer. The dorsal and ventral parts of the tail (left and right sides relative to the body axes of the trunk) form cellular fins, and the edge of each fin consists of a row of epidermal cells with a specific morphology (45). The left and right halves of the tail epidermis were exclusively derived from the L- and R-cells, respectively (*SI Appendix*, Fig. S1*G*). However, this did not clarify the origin of the midline fin edge cells. Our results showed that the R- and L-cells invariably gave rise to anterior and posterior portions of the fin edge cells, respectively (Fig. 2*E*). However, the posterior tip contained two cells derived from the R-cell. These results highlighted that L- and R-cells in the two-cell embryo show stereotyped asymmetries in their cell fates; this is in contrast to ascidian and vertebrate embryos.

Repetitive Asymmetric Ca^{2+} Waves Occur during Embryogenesis. Next, we tested whether the intracellular activity of the L- and R-cells was symmetric. Intracellular Ca^{2+} was monitored using a genetically encoded Ca^{2+} indicator (G-Camp8) (46). Time-lapse Ca^{2+} imaging revealed that asymmetric Ca^{2+} waves were present across the L–R axis in the two-cell embryos (Fig. 3 *A–C*). As shown in Fig. 3*B*, G-Camp8 fluorescence was elevated in one blastomere of the two-cell embryo. The cell-to-cell propagation of the Ca^{2+} wave passed through the center of the first cleavage plane (Fig. 3*C*) (n = 14 embryos). Each Ca^{2+} wave lasted 10 s. These Ca^{2+} waves repeated at intervals of several minutes. The firing points of the Ca^{2+} waves did not coincide with the first cleavage plane (Fig. 3 *D* and *E*, *SI Appendix*, Fig. S2, and Movie S3). The whole-embryo Ca^{2+} wave was also present in 4-cell, 8-cell, 16-cell, and 32-cell embryos, and even in the gastrula and neurula (Movie S4). However, it should also be noted that a recent Ca^{2+} imaging study in *O. dioica* revealed that the direction of the Ca^{2+} wave became roughly bilateral after the 16-cell stage (47). Hereafter, we will refer to this repetitive Ca^{2+} wave as Ca^{2+} oscillation.

In most chordate embryos, such as ascidians and mammalians, Ca^{2+} oscillation starts after fertilization and terminates after polar body extrusion (48–50). In contrast, in *O. dioica*, Ca^{2+} oscillation lasted through cleavage, gastrulation, and neurulation (*SI Appendix*, Fig. S3*A* and Movie S5), and was terminated at the early tailbud stage (~2 hpf). Intervals of Ca^{2+} waves varied between embryos (2 min 10 s to 4 min 45 s, n = 17 embryos), suggesting that Ca^{2+} oscillation has no relationship with the cell cycle. We observed two to three waves during the two-cell stage. Similarly, Ca^{2+} oscillation was also observed in unfertilized eggs (*SI Appendix*, Fig. S3 *B* and *C* and Movie S6) during metaphase

Downloaded at Palestinian Territory, occupied on December 7, 2021
www.manaraa.com

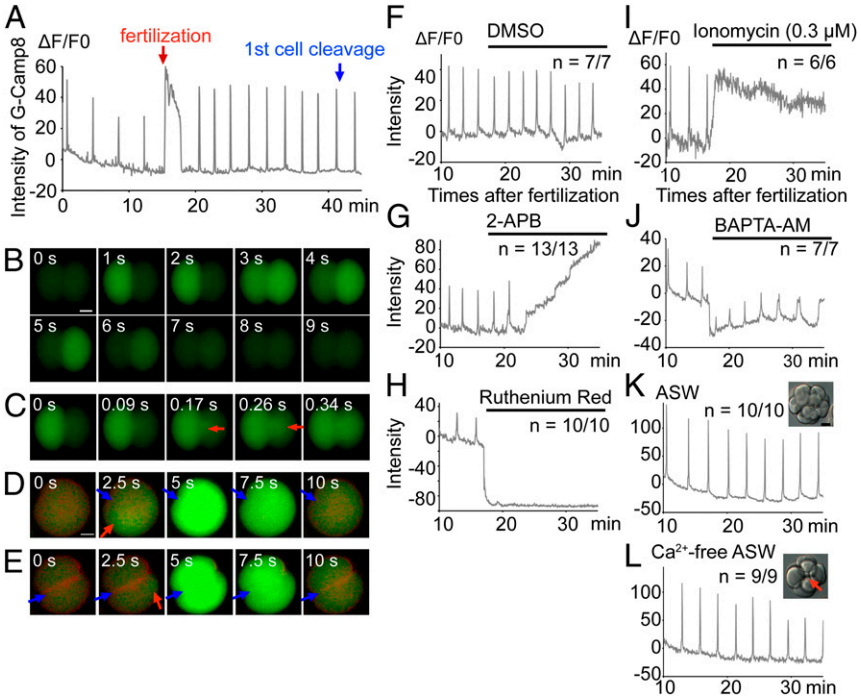

Fig. 3. Repetitive Ca^{2+} waves run asymmetrically along the L–R axis. (*A*) Time-course of intracellular Ca^{2+} levels, visualized using G-Camp8. Note that Ca^{2+} oscillation was observed before fertilization (red arrow) and after cleavage (blue arrow). (*B* and *C*) Sequential images of a Ca^{2+} wave in the two-cell embryo and low (*B*) and high (*C*) time-resolution. The wave was transmitted from one cell to another via the center of the cleavage plane (red arrows). (*D* and *E*) The firing point of the Ca^{2+} wave (red arrows) was not from the first cleavage plane (blue arrows). F-actin in the cleavage furrow was visualized using Lifeact-mCherry. Ca^{2+} waves before and after cleavage plane formation are shown in *D* and *E*, respectively. (*F–L*) Ca^{2+} oscillation is dependent on intracellular Ca^{2+} levels. Embryos were recorded beginning 10 min after fertilization. (*F–J*) Ca^{2+} oscillation was monitored for 20 min after the application of DMSO (*F*), 2-APB (*G*), Ruthenium red (*H*), ionomycin (*I*), or BAPTA-AM (*J*). (*K* and *L*) Time-lapse recordings were carried out immediately after transferring embryos into artificial seawater (*K*) or Ca^{2+}-free seawater (*L*). Cell-to-cell contacts became loose in Ca^{2+}-free seawater (*Inset*, red arrow). (Scale bars, 20 μm.)

of meiosis I (51). Accordingly, Ca^{2+} oscillation was not abrogated by cytokinesis or cyclin-dependent kinase 1 (CDK1) activity, as determined by treatment with cytochalasin B and roscovitine, respectively (*SI Appendix*,Fig. S4 *A* and *B*).

We next investigated whether the origin of the Ca^{2+} wave was the same in the L- and R-cells. If so, the direction of the Ca^{2+} wave could be considered one of the L–R pattering processes. To test this, embryos were reared up to the eight-cell stage after Ca^{2+} imaging at the two-cell stage. At the eight-cell stage, the left and right sides were distinguishable by cell size and geometry (Fig. 1*G*). Our results showed that the Ca^{2+} wave started from the L-cell in 71% of embryos, and from the R-cell in 29% of embryos, showing a significant difference ($P < 0.05$, binomial test, $n = 52$). However, as the morphological asymmetries of juvenile and adults are always consistent between individuals, the direction of the Ca^{2+} wave is likely not directly linked with L–R patterning. It is also unclear how the direction of the Ca^{2+} wave is determined in the two-cell embryo. One plausible explanation involves the sperm entry point, because the sperm aster forms the pacemaker of Ca^{2+} oscillation in ascidian embryos (48, 50). However, this was not observed in larvacean embryos, as cell-to-cell propagation of Ca^{2+} waves was also observed in parthenogenetic embryos lacking a sperm aster (*SI Appendix*, Fig. S4*C*) (52).

Ca^{2+} Oscillation Requires Intracellular Ca^{2+} Stores. To obtain insight into how Ca^{2+} oscillation is generated, embryos were treated with pharmacological inhibitors, a Ca^{2+} ionophore, and a Ca^{2+} chelator (Fig. 3 *F–J*). Dimethyl sulfoxide (DMSO) did not affect Ca^{2+} oscillation and embryonic development (Fig. 3*F*). 2-Aminoethoxydiphenyl borate (2-APB) and Ruthenium red, inhibitors of the inositol trisphosphate (IP3)- and ryanodine-sensitive Ca^{2+} channel in the endoplasmic reticulum, respectively, abrogated Ca^{2+} oscillation (Fig. 3 *G* and *H*). The 2-APB treatment gradually elevated basal G-Camp8 fluorescence, while Ruthenium red exposure lowered the signal intensity, suggesting that these two agents abrogated Ca^{2+} oscillation through distinct pathways. Treatment with ionomycin, a Ca^{2+} ionophore, elevated basal Ca^{2+} levels and disrupted Ca^{2+} oscillation (Fig. 3*I*). On the other hand, basal G-Camp8 fluorescence was decreased by BAPTA-AM, a chelator of Ca^{2+} (Fig. 3*J*). Despite this, Ca^{2+} oscillation was maintained after BAPTA-AM exposure. This result implies that Ca^{2+} oscillation was not directly dependent on "steady-state" Ca^{2+} concentrations. The effects of these agents on embryogenesis and laterality formation are discussed below.

To test the role of free Ca^{2+} in seawater, embryos were incubated in artificial seawater and Ca^{2+}-free seawater (Fig. 3 *K* and *L*). In Ca^{2+}-free seawater, the embryonic shape was abnormal (Fig. 3 *L*, *Insets*), probably because of the dissociation of cells within the vitelline membrane. However, Ca^{2+} oscillation was maintained (Fig. 3*L*). These results suggested that Ca^{2+} oscillation is regulated through intracellular endoplasmic reticulum-related mechanisms, but not by extracellular Ca^{2+}.

Larvaceans Lack *Nodal* and Show Right-Sided *Bmp.a* Expression. In chordates, the left-side expression of *Nodal* in the embryo directs L–R asymmetry. This is a conserved developmental process for L–R pattering in all chordate species studied to date. However, we did not find any *Nodal* homologs in the genome browser of Norwegian *O. dioica* (Oikobase, http://oikoarrays.biology.uiowa.edu/Oiko/) (53) or in our newly constructed genome and transcriptome databases of Japanese *O. dioica* (54) (sequence information is available from the ANISEED, https://www.aniseed.cnrs.fr/browser/). Phylogenic analyses indicated the presence of three TGF-β homologs, but none belonged to the branch of Nodal proteins

Downloaded at Palestinian Territory, occupied on December 7, 2021

www.manaraa.com

(Fig. 4*A*). These results suggest that *O. dioica* lacks the conventional *Nodal*-dependent L–R patterning mechanism. Consistent with a previous study, Pitx, a transcription factor that functions downstream of Nodal, did not show asymmetric expression (55).

The three TGF-β homologs were identified as BMP proteins (Fig. 4*A*), whose genes were designated *Bmp3*, *Bmp.a*, and *Bmp.b*. *Bmp.a* and *Bmp.b* were originally named *Bmp4* and *Bmp7* in the Oikobase, respectively (53). These two genes formed sister branches with the BMP2/4 and BMP5/7/8 subfamilies. Therefore, it is difficult to precisely determine their position on the phylogenic tree. Here, we renamed them *Bmp.a* and *Bmp.b*, following the nomenclature of tunicate genes (56). BLASTP analysis of Bmp.a and Bmp.b against the human protein database indicated the best-hit proteins as BMP2 and BMP5, respectively. Whole-mount in situ hybridization (WISH) detected the expression of *Bmp.a* in the right-ventral side of tailbud embryos (Fig. 4*B*) and hatched larvae (Fig. 4*D*). To confirm the orientation of *Bmp.a* expression, embryos were double-stained for a brain marker gene, *Pax6* (57). Positive *Bmp.a* signals were found on the right side of the trunk. In contrast, *Bmp.b* expression was observed on the left and right sides (Fig. 4 *C* and *E*).

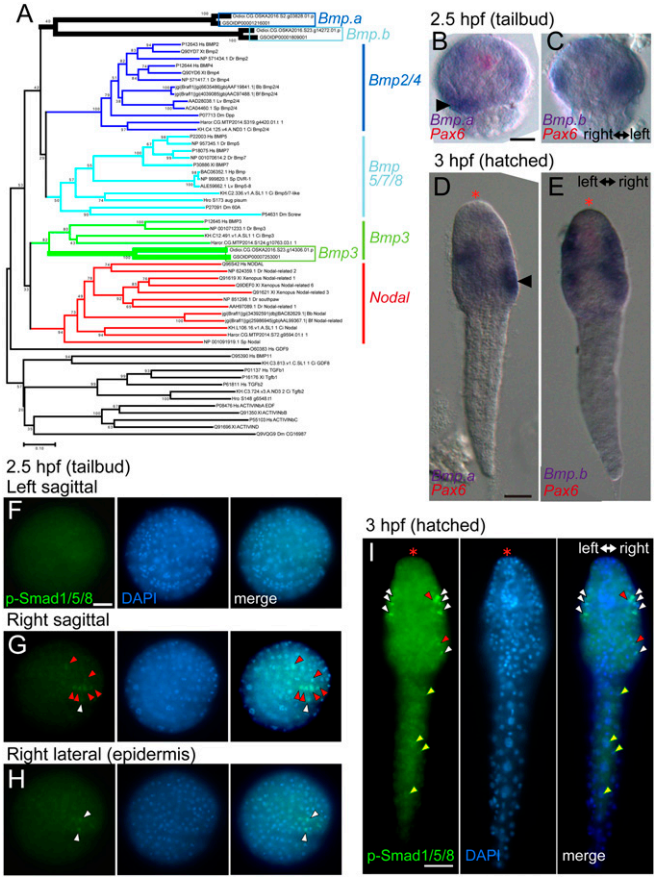

Fig. 4. The larvacean genome lacks *Nodal*, but bone morphogenic protein.a (*bmp.a*) shows right-sided expression. (*A*) Phylogenic tree of the TGF-β superfamily. Branches of Nodal proteins are labeled with red lines. Three Bmp homologs in *O. dioica* are labeled with rectangles. The expression of *Bmp.a* (*B* and *D*) and *Bmp.b* (*C* and *E*) was determined by in situ hybridization of prehatching tailbud embryos (*B* and *C*) (anterior views) and hatched larvae (*D* and *E*) (dorsal views). *Bmp.a* expression was observed on the right side (black arrowheads). Brain-specific expression of *Pax6* (red asterisks) was used for the orientation of embryos. (*F–I*) BMP signaling was detected predominantly on the right side. BMP was detected using an antibody against p-Smad1/5/8 (green). Nuclei were counterstained with DAPI (blue). (*F–H*) Right views of prehatching tailbud embryos (2.5 hpf). Pictures taken at three focus planes are shown. (*I*) Dorsal views of hatched larvae (3 hpf). Images show p-Smad1/5/8 staining (*Left*), DAPI counterstaining (*Center*), and merged images (*Right*). White and red arrowheads indicate signals in the epidermis and internal tissue, respectively. Yellow arrowheads indicate signals in the tail. Asterisks indicate the anterior tip of the larvae. (Scale bars, 20 μm.)

To confirm whether BMP signaling occurs predominantly on the right side, we used an antibody against phosphorylated Smad1/5/8 (p-Smad1/5/8). p-Smad1/5/8 is transported into the nucleus in response to BMP signaling. Nuclear p-Smad1/5/8 expression was confirmed in the larvacean (Fig. 4 *F–I* and *SI Appendix*, Fig. S5), consistent with previous observations in ascidians (58). Nuclear p-Smad1/5/8 signals were consistently lost after treatment with Dorsomorphin, a specific inhibitor of BMP receptor (*SI Appendix*, Fig. S5*A*). As shown in Fig. 4 *F–H*, we observed strong p-Smad1/5/8 signaling on the right side of prehatching tailbud embryos, primarily in the nuclei of internal cells and the epidermis. Similarly, p-Smad1/5/8 was detected in internal cells on the right side of hatched larvae (Fig. 4*I* and *SI Appendix*, Fig. S5*B*). Furthermore, moderate p-Smad1/5/8 expression was detected in the tail (Fig. 4*I* and *SI Appendix*, Fig. S5*B*), as well as the muscle, notochord, and tail epidermis. These results suggested that BMP signaling targets inner cells in the trunk and tail.

***Bmp.a*-Expressing Cells Are Descendants of the R-Cell.** We next determined whether the *Bmp.a*-expressing cells originated in the epidermis or endoderm, as well as whether they were descendants of the L- or R-cells of the two-cell embryo. As shown in Fig. 1*G*, L–R and animal–vegetal orientations can be defined based on cell size and cell contacts after the eight-cell stage. Eight-cell embryos were treated with cytochalasin B to block cell division, and the expression of *Brachyury* and *Bmp.a* was monitored at the hatching stage (3 hpf) (Fig. 5*A*). Brachyury is a key transcription factor for notochord formation (59). *Brachyury* mRNA was detected in anterior cells of the vegetal hemisphere (A-lines in Fig. 5*B*), which includes cells with a notochord fate (4). On the other hand, *Bmp.a* mRNA was detected in anterior cells of the animal hemisphere (a-lines in Fig. 5*C*). It is known that the frequency of cell-type specific marker expression is reduced in cleavage-arrested embryos compared to that in normal embryos (60). Accordingly, *Brachyury* expression was detected in about 20% of the L- (A) and R-cells (A) in all embryos (Fig. 5*D*). In contrast, *Bmp.a* expression was detected in 40% of the R-cells (a), but none of the L-cells (a) (Fig. 5*D*). In a similar experiment using the two-cell embryo, *Bmp.a* was expressed in one of the two cells, although the left and right side could not be distinguished (Fig. 5 *E–G*). In contrast, *Brachyury* expression was detected in both blastomeres in ∼40% of embryos. These results suggested that *Bmp.a* is expressed in descendants of the R-cell.

This finding was then confirmed through an independent approach. *Bmp.a* expression in the tailbud embryos was detected by fluorescent in situ hybridization using FastRed and nuclei counterstained with DAPI (Fig. 5*H*). The spatial distribution of *Bmp.a*-expressing cells was compared with *z*-stack images in which the L- and R-descendants were labeled with nls-Kaede, using the position of some landmark cells with defined nucleus sizes (Fig. 5*I* and Movie S7). All *Bmp.a*-expressing cells were identified as descendants of the R-cell, but not the L-cell (Fig. 5 *H* and *I*).

Ca^{2+} Oscillation Is Required for *Bmp.a* Expression. In vertebrate embryos, Ca^{2+} pulses have been observed in the cilia of cavities, primarily node in mice or its homologs in other animals; Ca^{2+} pulses in the cilia are required for *Nodal*-dependent L–R patterning (20, 21). In larvaceans, it was recently reported that the knockdown of gap junction proteins caused uncoordinated Ca^{2+} wave propagation between cells and abnormal embryogenesis (47). We hypothesized that Ca^{2+} oscillation might have a role in right-sided *Bmp.a* expression. Embryos were treated with ionomycin

Downloaded at Palestinian Territory, occupied on December 7, 2021
www.manaraa.com

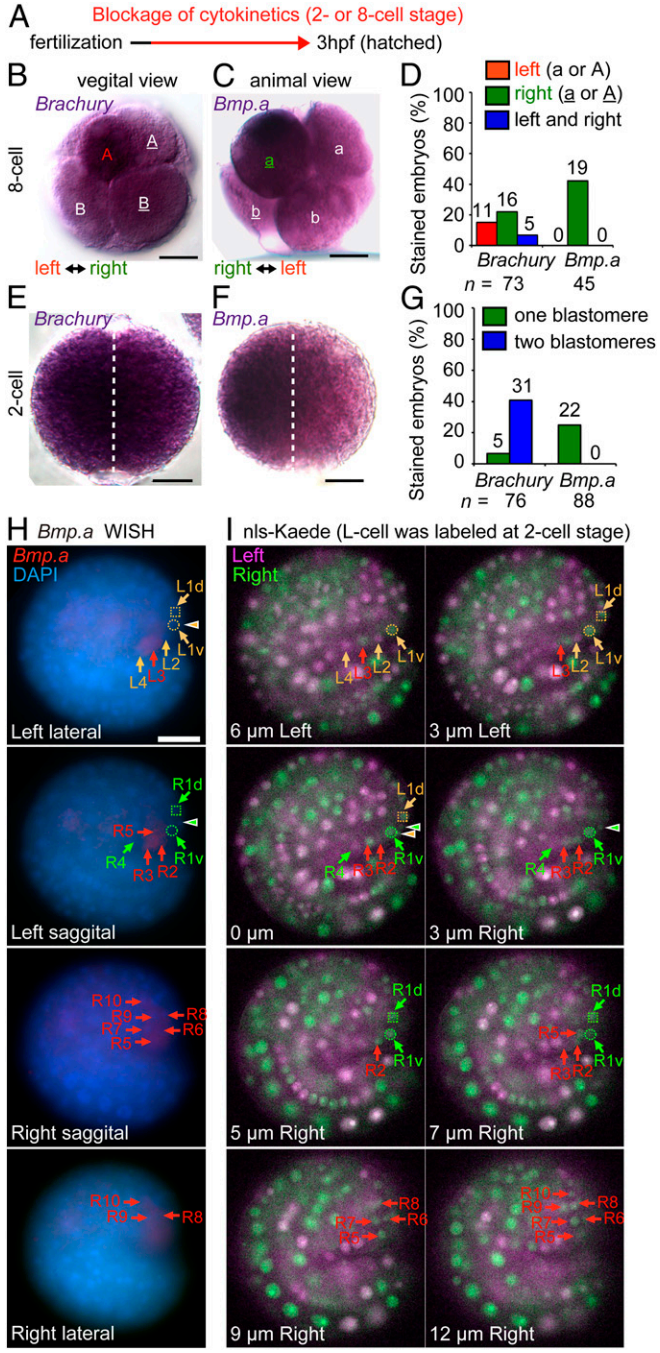

Fig. 5. *Bmp.a*-expressing cells are descendants of the R-cell. (*A*–*G*) Two- or eight-cell embryos were cultured with cytochalasin B to block cell division. (*A*) Experimental design. In situ hybridization of *Brachyury* and *Bmp.a* mRNAs was carried out at the hatching stage (3 hpf). (*B* and *C*) *Brachyury* (*B*) and *Bmp.a* (*C*) mRNA levels were detected in anterior cells in the vegetal hemisphere (A-line) and animal hemisphere (a-line), respectively. Left and right orientation is reversed in the animal view. (*D*) Proportion of signal-positive blastomeres in *B* and *C*. The number of positive embryos is indicated above each bar. (*E*–*G*) Cleavage-arrested two-cell embryos analyzed as in *B*–*D*. Dotted lines indicate the first cleavage plane. The orientation of these embryos is unknown as they are cleavage-arrested at the two-cell stage. (*H* and *I*) Pictures of tailbud embryos (2.5 hpf) were taken at four and eight focus planes, respectively. Right views. The trunk is up, and the tail is down. (*H*) *Bmp.a* mRNA was visualized with FastRed. Nuclei were counterstained with DAPI (blue). A pair of small nuclei (left and right nuclei indicated with orange and green arrowheads, respectively) was used as the landmark for cells in the medial plane. Four adjacent epidermal cells surrounded the landmark, which are labeled as dorsal left (L1d), dorsal right (R1d), ventral left (L1v), and ventral left (R1v). Other left (L) and right (R) epidermal cells are sequentially numbered and labeled with orange and green letters, respectively. Red letters indicate *Bmp.a* mRNA$^+$ cells, which are located within green nls-Kaede (R-origin) cells in *I*. (*I*) The L-cell of the two-cell embryo was labeled with photoconverted red nls-Kaede (red fluorescence). The L- and R-descendants are indicated as described in *H*. (Scale bars, 20 μm.)

(1 μM), 2-APB, and Ruthenium red. While these agents effectively disrupted Ca^{2+} oscillation (Fig. 3 *G*–*I*), they also abrogated cell cleavage and caused abnormal embryogenesis. Therefore, to address this issue, experiments were performed in the presence of cytochalasin B from the eight-cell stage to keep the embryonic configuration constant and minimize the indirect effects of the drugs. As shown in Fig. 6*A*, *Bmp.a* expression was abrogated in embryos treated with these inhibitors. However, *Brachyury* expression was not affected (Fig. 6*A*). We identified a significant reduction in the proportion of *Bmp.a*-, but not *Brachyury*-, expressing embryos (Fig. 6*B*). Similarly, quantitative real-time PCR (qPCR) showed decreases in the expression of *Bmp.a* after inhibitor treatments (Fig. 6*C*), although *Brachyury* expression was unaffected (Fig. 6*D*).

These results suggest that the disruption of Ca^{2+} oscillation potentially abrogated *Bmp.a* expression. However, there remain two other possibilities: 1) Pharmacological treatment may have affected *Bmp.a* expression and disrupted embryogenesis, and 2) *Bmp.a* expression is dependent on "steady-state" Ca^{2+} concentrations rather than Ca^{2+} oscillation. Thus, we optimized the concentration of ionomycin and found that 0.1 μM and 0.3 μM did not affect embryogenesis; more than 90% of embryos developed into the tailbud (Fig. 6*F*). Treatment with 0.3 μM ionomycin did not affect the location of the nerve cord on the left side based on morphology (Fig. 6*E*). However, 0.3 μM ionomycin was sufficient to disrupt Ca^{2+} oscillation (Fig. 3*I*) and reduce the proportion of *Bmp.a*-, but not *Brachyury*-, expressing embryos (Fig. 6 *E* and *G*). Furthermore, treating embryos with an inhibitor of Ca^{2+}/calmodulin-dependent protein kinase-II (CaMK-II), KN93, significantly decreased the number of *Bmp.a*-expressing embryos (*SI Appendix*, Fig. S6*A*). KN93-treated embryos developed into the tailbud. These results support that Ca^{2+} oscillation is required for *Bmp.a* expression.

Next, we tested whether steady-state Ca^{2+} concentrations were important for *Bmp.a* expression (Fig. 6 *H*–*J*) using BAPTA-AM, a Ca^{2+} chelator. As shown in Fig. 3*J*, intracellular Ca^{2+} was lowered by BAPTA-AM treatment. Nonetheless, Ca^{2+} oscillation was sustained, and more than 80% of embryos developed into a tailbud (Fig. 6*I*). BAPTA-AM treatment did not affect right-sided *Bmp.a* expression or *Brachyury* expression in the notochord (Fig. 6*H*). Therefore, it is likely that an intracellular steady-state Ca^{2+} level is not the primary regulator of *Bmp.a* expression. Instead, it is likely that Ca^{2+} oscillation has a role in activating *Bmp.a* expression.

To determine the sensitive period, we disrupted Ca^{2+} oscillation for different durations or during different developmental periods using 2-APB, an inhibitor of the IP3 receptor (*SI Appendix*, Fig. S6 *B* and *C*). First, 2-APB treatment was initiated at four stages: 0.5 hpf, 1 hpf, 1.5 hpf, and 2 hpf. *Bmp.a* expression in each group was then determined by qPCR. Exposure from 2 hpf was the least effective among the groups (*SI Appendix*, Fig. S6*B*). This was expected, because Ca^{2+} oscillation terminates at around 2 hpf (*SI Appendix*, Fig. S3*A*). Next, the duration of treatment was fixed at 1 h. Embryos were treated at three different periods: 0.5 to 1.5 hpf, 1 to 2 hpf, and 1.5 to 2.5 hpf, although we could not confirm whether the drug was completely washed out (*SI Appendix*, Fig. S6*C*). The results indicated that 1 to 2 hpf was the most effective period (less than 10% that of the DMSO-control group).

Downloaded at Palestinian Territory, occupied on December 7, 2021

www.manaraa.com

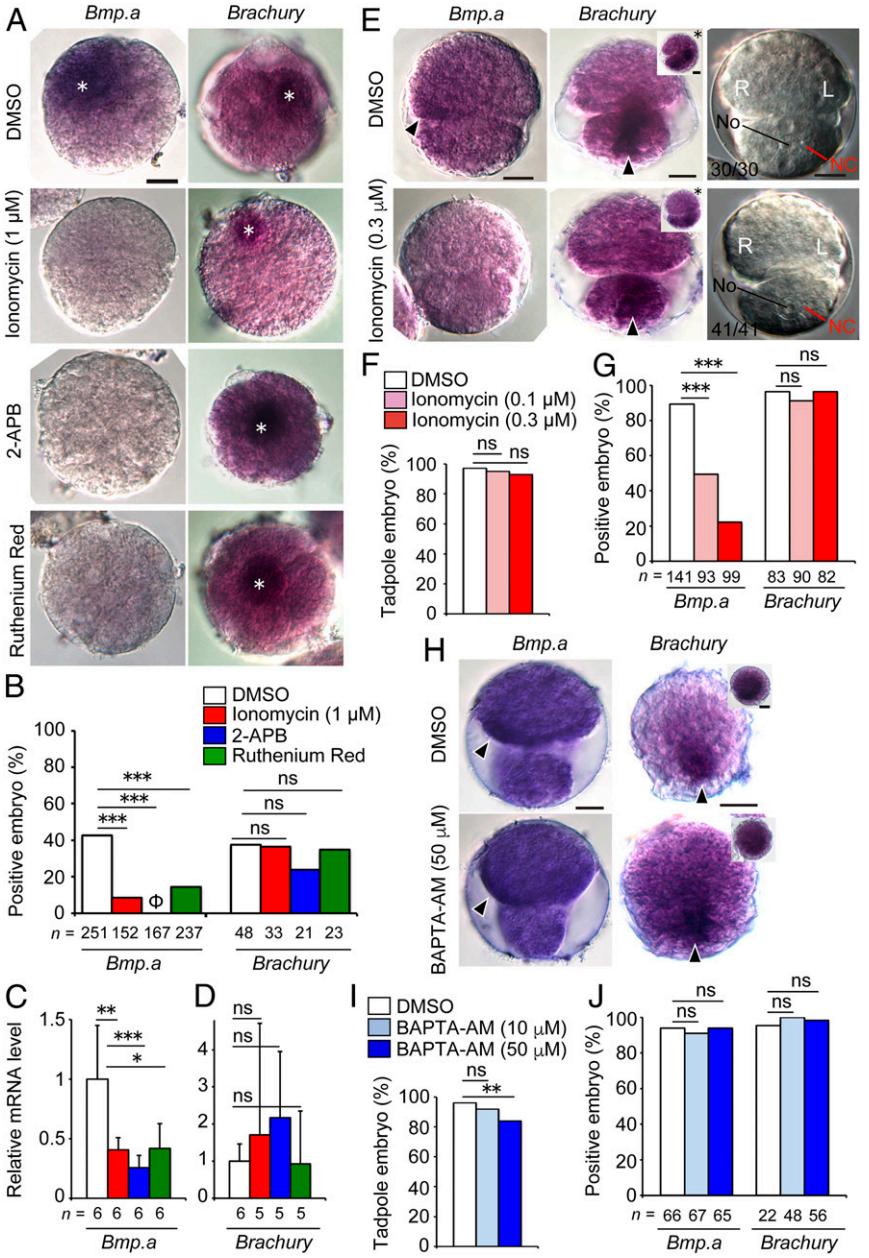

Fig. 6. Disruption of Ca^{2+} oscillation abrogates *Bmp.a* expression. (*A*) Eight-cell embryos were treated with cytochalasin B with ionomycin or the indicated inhibitors at the eight-cell stage. *Bmp.a* (*Left*) and *Brachyury* (*Right*) mRNA levels were detected at the hatching period (3 hpf). Asterisks indicate in situ hybridization signals. (*B*) Proportions of positive embryos in *A* (Fisher's exact test). (*C* and *D*) qPCR analyses of *Bmp.a* (*C*) and *Brachyury* (*D*) expression. Expression levels were normalized to that of cytoplasmic *actin* (Student's *t* test). (*E–G*) *Bmp.a* expression was abrogated by treatment with low concentrations (0.1 to 0.3 μM) of ionomycin. Embryos developed into normal-shaped tailbud embryos without cleavage arrest. (*E*) Anterior view. Arrowheads indicate *Bmp.a* expression on the right side (*Left* images) or *Brachyury* expression in the notochord (*Center* images). *Insets* represent lateral views. Right images highlight the nerve cord (NC) on the left side of the notochord (No). Numbers indicate the ratio of tailbud embryos with this morphological asymmetry of the NC. (*F* and *G*) The proportion of normal-shaped tailbud embryos (*F*) and positive embryos (*G*) (Fisher's exact test). (*H–J*) Low steady-state Ca^{2+} levels did not affect *Bmp.a* expression. (*H*) Embryos were treated with BAPTA-AM. Anterior views. Arrowheads indicate *Bmp.a* expression on the right side (*Left* images) or *Brachyury* expression in the notochord (*Right* images). *Insets* represent lateral views. (*I* and *J*) Proportion of normal-shaped tailbud embryos (*I*) and positive embryos (*J*) (Fisher's exact test). (Scale bars, 20 μm.) $*P < 0.05$, $**P < 0.01$, $***P < 0.001$, ns, not significant.

BMP Signaling Plays a Suppressive Role in Nerve Gene Expression. We next investigated whether BMP signaling affects neural gene expression. BMPs are an evolutionally conserved protein family that control D–V patterning and neural formation (12, 13). In vertebrates, activating BMP signaling has been shown to ventralize embryos, resulting in the loss of neural cell differentiation (12, 13). In ascidians, however, the embryo lacks an organizer, and BMP signaling is not required for central nervous system formation (61). As mentioned above, when *Bmp.a* expression was initiated in the tailbud embryos (Fig. 4*B*), the tail nerve cord was formed on the left side (Fig. 1 *H* and *I*). We therefore investigated whether BMP signaling plays a role in neural gene expression to clarify the mechanisms through which larvae maintain or restrict nerve cord differentiation. Embryos were treated with Dorsomorphin, an inhibitor of the BMP receptor. Given that right-sided *Bmp.a* expression was observed from the tailbud stage (Fig. 4*B*), Dorsomorphin

Downloaded at Palestinian Territory, occupied on December 7, 2021
www.manaraa.com

was applied at the early tailbud stage. Dorsomorphin-treated larvae displayed ectopic expression of the neural markers *Pax6* (Fig. 7*A*), glutamic acid decarboxylase (*GAD*), and *galanin* (Fig. 7*B*). *Pax6* is expressed specifically in the anterior brain (57). Ectopic *Pax6* expression was observed in the tail region as well as the trunk in all treated larvae. This was also the case for *GAD* and *galanin*, which are usually expressed in the left tail ganglion in normal embryos (38) (Fig. 7*B*). However, the effect of Dorsomorphin was gene-specific, as few changes were observed in the expression of choline acetyltransferase (*ChAT*), another marker of neural cells in the tail (38, 39) (Fig. 7*B*). qPCR analysis also showed increases in *Pax6* expression upon Dorsomorphin treatment (Fig. 7*C*). To verify these results using a different approach, *Bmp.a* expression was knocked down by double-stranded DNA (dsDNA)-mediated gene knockdown (DNAi) (62). *Bmp.a* knockdown also caused ectopic *Pax6* expression and elevated *Pax6* mRNA levels (*SI Appendix*, Fig. S7).

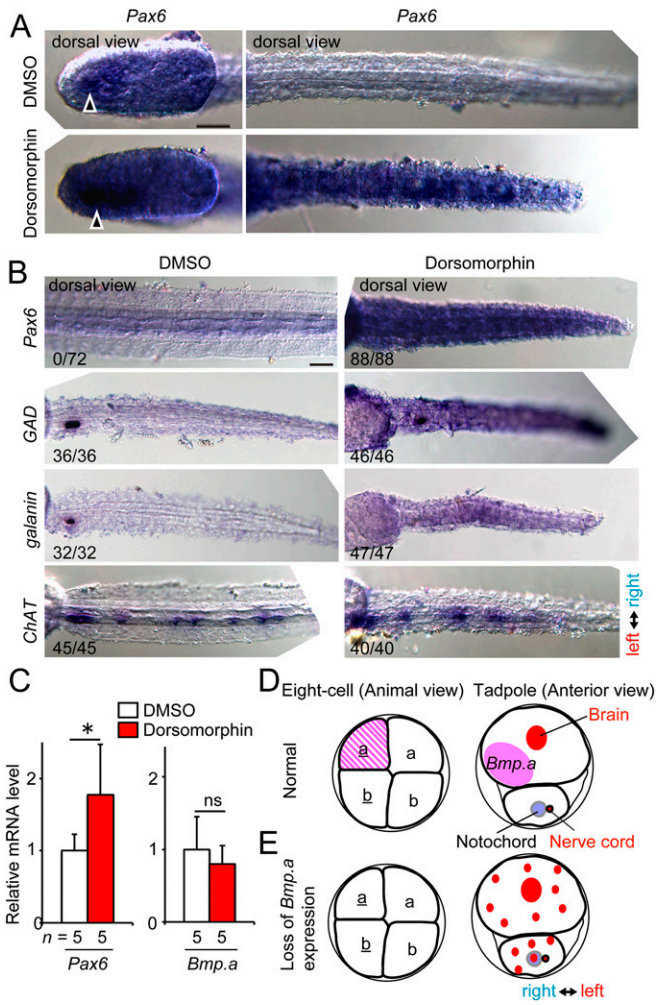

Fig. 7. Blockage of BMP signaling induces ectopic brain marker expression. (*A* and *B*) WISH of *Pax6* (a marker gene for the anterior brain), as well as *GAD*, *galanin* (marker genes for the tail ganglion), and *ChAT* (a marker gene for the tail nerve cord neurons). Prehatching larvae were treated with dorsomorphin, a BMP inhibitor. (*A*) Larvae at 2 h after hatching (5 hpf). (*B*) Larvae after organogenesis (8 hpf). Dorsal views. (*C*) qPCR analyses of *Pax6* and *Bmp.a* expression, normalized to that of *β-tubulin* (Student's *t* test, $*P < 0.05$). (*D*) Model of L–R patterning in larvacean embryo. *Bmp.a* expression occurred in the descendants of the right-anterior animal cell (a-line, hatched). The right-sided BMP signal restricted neural gene expression on the left side. (*E*) L–R patterning was abrogated when *Bmp.a* expression was lost. (Scale bars, 20 μm.)

These results suggest that BMP signaling has a suppressive role in the expression of neural genes such as *Pax6* in larvaceans.

Discussion

In this study, we showed that the larvacean *O. dioica* is a chordate species lacking *Nodal* that displays an unusual L–R patterning process requiring Ca^{2+} oscillation for right-sided *Bmp.a* expression. Our analyses also show that *Bmp.a*-expressing cells are exclusively derived from right-anterior animal cells, which correspond to the "a" cell of the eight-cell embryo that originates from the R-cell. These results expand on the monumental findings of Delsman (1), who initially described the L–R asymmetry of cellular arrangement in larvaceans as early as the four-cell stage, and provide insights into its relationship with morphological L–R differences in the larval body.

Our results indicated that the cell fates of the L- and R-cells were different. Tracing the descendants of the L- or R-cell demonstrated that even symmetric organs in larvae show consistent asymmetry in their L- and R-origins. For example, bilateral giant cells in the endostyle were descendants of the L-cell only. As shown by the generation of a mirror-imaged trunk epidermis, L- and R-descendants consistently invaded by crossing the median plane (4, 33). This is in contrast to ascidians, in which one blastomere in the two-cell embryo may give rise to the left or right half of tadpole larvae (40), and for which the endodermal cell lineages have symmetric tissue fates during metamorphosis (41). Asymmetric cleavage patterns and asymmetric cell contacts at the four-cell stage may be more similar to those observed during spiral cleavage in snails (29) or during the asymmetric arrangement of the four anterior (AB) blastomeres of *Caenorhabditis elegans* embryos (63), rather than those of chordates. Intriguingly, *C. elegans* also lacks *Nodal*.

In cleavage-arrested embryos at the two-cell stage, *Bmp.a* was expressed in one of the two cells. This implies that there are intrinsic mechanisms for cell-autonomous right-biased *Bmp.a* expression, in which a certain maternal factor could be differentially inherited by the L- and R-blastomeres. However, this was not confirmed because the left and right side could not be distinguished in the two-cell embryos.

Ca^{2+} imaging revealed that Ca^{2+} oscillation continued beyond gastrulation and neurulation, and was observed even before fertilization, unlike what is seen in ascidians and vertebrates (48–50). Moreover, the Ca^{2+} wave was also controlled through a process distinct from those in other chordates. For example, sporadic Ca^{2+} pulses arise independently in each cell in the gastrulae of ascidian species (64, 65). In contrast, Ca^{2+} waves run through the whole embryo until early tailbud in larvaceans. However, our results do not support the requirement for consistent Ca^{2+} oscillation for normal embryogenesis. A low concentration of ionomycin abrogated Ca^{2+} oscillation, but most embryos still developed the tailbud shape.

On the other hand, the present results showed that right-sided *Bmp.a* expression requires Ca^{2+} oscillation. Ca^{2+} oscillation has been shown to be necessary for the expression of certain genes in cell culture (66). In mouse and zebrafish, it has been proposed that repetitive Ca^{2+} pulses are generated via ciliary Ca^{2+} channels for left-sided *Nodal* expression and consequent L–R asymmetry (20, 21), highlighting the role of Ca^{2+} signaling in L–R patterning. However, our results did not precisely match the model established in vertebrates. First, the generation of Ca^{2+} oscillation was not dependent on the intake of Ca^{2+} ions from extracellular fluid, unlike in vertebrates (20, 21). Second, the *O. dioica* embryo does not have cilia. Third, Ca^{2+} oscillation runs through the entire embryo. Finally, *O. dioica* lacks the *Nodal*-dependent L–R patterning mechanism. The direction of the wave in cleavage-stage embryos varied between individuals and was not precisely correlated with the L–R axis. Therefore, Ca^{2+} oscillation should be considered to permit, rather than direct, *Bmp.a* expression.

Downloaded at Palestinian Territory, occupied on December 7, 2021
www.manaraa.com

BMP has a suppressive effect on *Pax6*, *GAD*, and *galanin* gene expression. p-Smad1/5/8 immunostaining indicated that BMPs were expressed predominantly on the right side. p-Smad1/5/8 was also detected in the tail. Because the tail nerve cord was already formed on the left side when right-sided *Bmp.a* expression was initiated, it is likely that BMP signals are utilized for the maintenance, rather than initiation, of tail nerve cord growth. BMP signaling is conserved for D–V patterning and the suppression of neural formation in the ventral side in all vertebrates (12, 13). Thus, we propose a model in which BMP signaling may be coopted to restrict neural gene expression on the left side in larvaceans (Fig. 7 *D* and *E*). It is well established that the D–V axis shows 180° inversion between *Drosophila* and *Xenopus* embryos in relation to the spatial pattern of BMP signaling (11–13). Our data could be regarded as an example of induction of a 90° rotation for L–R patterning by D–V patterning and BMP expression in larvaceans.

In summary, our study provides evidence of a chordate species that lacks *Nodal* and utilizes Ca^{2+} oscillation and *Bmp.a* for L–R patterning. The larvacean provides a valuable research model to study the divergence of the L–R patterning process in tadpole body formation. However, several important questions remain unanswered. First, it is uncertain when and how the descendants of the L- and R-cells diverge. As mentioned above, there is minimal evidence that the direction of the Ca^{2+} waves is a determinative factor. Transcriptomic analysis of the L- and R-cells and their descendants should also be performed in the future. Furthermore, it remains to be determined how the cell arrangement becomes asymmetric at the four-cell stage, and how this early asymmetry affects late asymmetry of larval morphologies. This may be clarified through the characterization of intracellular components that control spindle orientation. Finally, it will be important to determine how these early asymmetries eventually lead to the left twisting of the tail nerve cord.

Methods

Animals and Reagents. *O. dioica* were cultured over 350 generations for more than 6 y in an inland laboratory at Osaka University at 20 °C, as previously described (3, 58). Larvaceans hatched at 3 hpf, and underwent complete organogenesis and formed fully functional bodies by 10 hpf. The anatomical terms used are according to those in the latest version of the anatomical atlas (7). All experiments were repeated at least twice independently. Embryonic cells in the eight-cell embryo were named following the nomenclature used by Delsman (1).

In Situ Hybridization and Immunostaining. cDNA sequences of the genes of interest were identified by BLAST using the public genome database of the Norwegian *O. dioica* population (Oikobase: http://oikoarrays.biology.uiowa.edu/Oiko/index.html) and our own transcriptome database of a Japanese *O. dioica* population constructed by the de novo assembly of RNA sequencing data from eggs and larvae (54). Sequence information of genes used in this study has been available from the public genome database (ANISEED: https://www.aniseed.cnrs.fr/browser/). Primer pairs were designed to amplify cDNA fragments; their sequences and the identifiers for genes used in the present study are also shown in *SI Appendix*, Table S1.

WISH was carried out following our recently developed protocol (67). Digoxigenin (DIG)- or fluorescein-labeled RNA probes were synthesized with SP6 or T7 RNA polymerase (Roche Diagnostics). Signal detection was carried out using nitro blue tetrazolium/5-bromo-4-chloro-3-indolyl phosphate (NBT/BCP). For double staining with FastRed (Sigma Aldrich), embryos were treated with 0.1 M glycine (pH 2.2) for 30 min to terminate the NBT/BCIP reaction and washed with PBS containing 0.1% Tween-20 (PBSTw, pH 7.4). Specimens were then incubated with blocking buffer and 1:3,000 antifluorescein-alkaline phosphatase (Roche Diagnostics) at 4 °C overnight. The FastRed chromogenic reaction was carried out under the same conditions used for the NBT/BCP reaction.

To detect the activation of the BMP signaling pathway, embryos and larvae were fixed as previously described (67). After treatment with with 3% H_2O_2 for 30 min, samples were incubated with a rabbit polyclonal antibody targeting a synthetic phosphopeptide derived from human Smad1 (Abcam; ab97689; 1:25,000) in Can-Get-Signal Immunostain Solution B (Toyobo) at 4 °C overnight. This antibody was selected because *Oikopleura* Smad has the same C-terminal amino acid sequence as human Smad1. The signal was visualized with a tyramide signal amplification kit (Invitrogen) using horseradish peroxidase-conjugated goat anti-rabbit IgG (Histofine Sample Stain MAX PO; Nichirei Biosciences) and Alexa Fluor 488-conjugated tyramide. Specimens were washed three times in PBSTw and mounted in VECTASHIELD with DAPI (Funakoshi Co.) to counterstain nuclei. Alternatively, samples were stained with 0.1 μg/mL DAPI in buffer and observed with a noncover water lens. For tubulin immunostaining, embryos were fixed with 100% methanol, followed by incubation with 100% ethanol for 30 min. After washing with PBSTw, samples were incubated with the antitubulin antibody YL1/2 (NB600-506; 1:1,000; Novus Biologicals) in PBSTw overnight. Samples were then incubated with the secondary antibody (Alexa Fluor 488-conjugated goat anti-rat IgG; 1:1,000) overnight.

Live Imaging. The mMESSAGE mMACHINE kit and Poly (A) Tailing kit (Ambion) were used to synthesize mRNAs encoding nls-Kaede for cell fate tracing (33), G-Camp8 for Ca^{2+} imaging (gift from J. Nakai and M. Okura, Saitama University, Saitama, Japan), and Lifeact-mCherry for F-actin visualization. The *G-Camp8* cDNA sequence was amplified by PCR (forward primer, 5′-TATATCTCGAGAAGCTTATCTCGCCACCATGGGTTCTC-3′; reverse primer, 5′-TATATAGCGGCCGCTCTACAAATGTGGTATGGCTG-3′), and subcloned into the XhoI/NotI sites of the pSD64TF-H2B-EGFP vector (32). The Lifeact-mCherry construct was generated by PCR mutagenesis of the pSD64TF-H2B-mCherry vector (32) (forward primer, 5′-AATTCGAAAGCATCTCAAAGGAAGAAACGGTA-CCGCGGGCCCGG-3′; reverse primer, 5′-TCTTGATCAAATCTGCGACACCCATGGT-GGCCAGAATTCG-3′). These primers were designed to replace the H2B sequence with the Lifeact sequence.

For live imaging, the ovarian microinjection of mRNA was performed at ∼12 h before spawning, as described previously (32, 58). The injected mRNAs are incorporated into multiple oocytes because each pro-oocyte is connected to a shared cytoplasm through pores known as the ring canal (51), and mRNA diffuses within the syncytial cytoplasm to form a concentration gradient and is eventually brought into 20 to 30% of spawned eggs (32, 58). Eggs or embryos with the required fluorescence intensity were selected and used for imaging.

Labeling L- or R-Cells with Photoconvertible nls-Kaede. To convert nls-Kaede fluorescence from green to red, one blastomere in the two-cell embryo was exposed to UV light for 3 s at least 5 min after the first cleavage under an Olympus BX-61 microscope with a LUMPlanFL N 40×/0.80 water immersion lens (Olympus). The field iris diaphragms were adjusted to cover one blastomere of the embryo. The distribution of labeled nuclei in descendant cells (red cells) was monitored at 10 hpf using a DeltaVision wide-field microscope (GE Healthcare). To immobilize hatched larvae during data collection, animals were mounted on agarose gel plates or attached to the bottom of glass-bottomed dishes (33). At least three independent observations were carried out for both L- and R-cell-labeled individuals.

Time-Lapse Imaging of Intracellular Ca^{2+} Levels. G-CaMP8 mRNA was injected into an immature ovary together with Lifeact-mCherry mRNA as an injection marker. For time-lapse imaging, vitelline membranes of injected eggs were attached to a glass-bottomed dish coated with poly-L-lysine. G-CaMP8 fluorescence was recorded using an Olympus BX61 microscope equipped with a LUMPlanFL N 40×/0.80 water immersion lens. Images were acquired at 2.5-s intervals unless otherwise stated. Relative changes in fluorescence intensity ($\Delta F/F_0$) were calculated as previously described (68). Signal intensity was measured using ImageJ. *F* values were calculated as follows: The signal intensity outside the eggs was subtracted from that in the eggs, and the median *F* value for >100 flames of the baseline period was defined as F_0. $\Delta F/F_0$ was measured for each egg using the equation $\Delta F/F_0 = [F - F_0]/F_0$.

Pharmacological Inhibitors. Animals were treated with 0.1 to 1 μM ionomycin (a calcium ionophore; Cayman Chemical), 50 μM 2-APB (an IP3 receptor inhibitor; Wako Pure Chemical), 150 μM Ruthenium Red (a ryanodine receptor inhibitor, Wako Pure Chemical), 50 μM BAPTA-AM (a calcium chelator, Nacalai Tesque), 3 μM Dorsomorphin (a BMP receptor inhibitor, Wako Pure Chemical), 20 μM roscovitine (a CDK-1 inhibitor, Cell Signaling Technology), 2.5 μg/mL cytochalasin B (a cytokinesis inhibitor, Sigma Aldrich), or 100 μM KN-93 (a CaMK-II inhibitor, Tokyo Chemical Industry). DMSO (solvent, 0.2 to 0.5%) was used as a control.

DNAi. dsDNA-induced gene knockdown (62) was adopted for the knockdown of *Bmp.a*. A PCR product covering more than half of the BMP.a protein-coding region was amplified, purified, and injected into the ovary.

Downloaded at Palestinian Territory, occupied on December 7, 2021
www.manaraa.com

Next, 0.5 μg/μL mRNA encoding Lifeact-EGFP or Lifeact-mCherry was coinjected as an injection marker together with 0.2 μg/μL dsDNA. Only eggs that had EGFP or mCherry fluorescence were used for analysis. In some experiments, a PCR product encoding the fluorescent protein Kaede was used as control dsDNA.

qPCR. Total RNA from each sample was purified from 20 eggs with NucleoSpin RNA XS (Macherey-Nagel) and converted to cDNA with PrimerScript RT Reagent with gRNA Eraser (Takara Bio) according to the manufacturer's protocol. qPCR was performed with the ABI 7300 Real-Time PCR System (Applied Biosystems) using the TB Green Advantage qPCR Premix (Takara Bio). PCR was performed for 40 cycles of 95 °C for 15 s, 60 °C for 30 s, and 72 °C for 30 s. Three to five separate samples were analyzed for each experiment. The amplified products were confirmed by a melting curve and gel electrophoresis. The mRNA expression levels of *Bmp.a* and *Brachyury* were normalized against *β-tubulin* or cytoplasmic *actin* as an internal control. The oligonucleotide sequences used for qPCR are summarized in *SI Appendix*, Table S1. Primers were designed to produce PCR products with a size of 80 to 250 bp.

Statistical Analysis. Statistical analyses were carried out using Student's *t* test, the χ^2 test, Fisher's exact test, the binomial test, or one-way ANOVA with Tukey's post hoc test. A value of $P < 0.05$ was considered statistically significant.

ACKNOWLEDGMENTS. We thank Ms. Masae Suzuki, Ms. Keiko Kayahara, and the students in our laboratory for their assistance in the laboratory culture of *Oikopleura dioica*; and Editage (https://www.editage.com/) for English language editing. This work was supported by Japan Society for the Promotion of Science Grants-in-Aid for Scientific Research 24870019, 26840079, 18K06256, and 18H04763 (to T.A.O.) and 26650079, 15H04377, 16K14735, 17KT0023, and 19H03234 (to. H.N.); and research grants from the Inamori Foundation (2015), the Kato Memorial Research Foundation (2015–2016), the Sumitomo Foundation (2016–2017), and Japan Foundation for Applied Enzymology (2017, 2019) to T.A.O.

1. H. C. Delsman, Beiträge zur Entwicklungsgeschichte von *Oikopleura dioica*. *Verh. Rijksinst. Onderz. Zee.* **3**, 1–24 (1910).
2. S. Fujii, T. Nishio, H. Nishida, Cleavage pattern, gastrulation, and neurulation in the appendicularian, *Oikopleura dioica*. *Dev. Genes Evol.* **218**, 69–79 (2008).
3. H. Nishida, Development of the appendicularian *Oikopleura dioica*: Culture, genome, and cell lineages. *Dev. Growth Differ.* **50** (suppl. 1), S239–S256 (2008).
4. T. Stach, J. Winter, J.-M. Bouquet, D. Chourrout, R. Schnabel, Embryology of a planktonic tunicate reveals traces of sessility. *Proc. Natl. Acad. Sci. U.S.A.* **105**, 7229–7234 (2008).
5. R. Fenaux, "Anatomy and functional morphology of the Appendicularia" in *The Biology of Pelagic Tunicates*, Q. Bone, Ed. (Oxford University Press, 1998), pp. 25–34.
6. P. Burighel, C. Brena, Gut ultrastructure of the appendicularian *Oikopleura dioica* (Tunicata). *Invertebr. Biol.* **120**, 278–293 (2001).
7. T. A. Onuma, M. Isobe, H. Nishida, Internal and external morphology of adults of the appendicularian, *Oikopleura dioica*: An SEM study. *Cell Tissue Res.* **367**, 213–227 (2017).
8. C. J. Boorman, S. M. Shimeld, The evolution of left-right asymmetry in chordates. *BioEssays* **24**, 1004–1011 (2002).
9. N. Hirokawa, Y. Tanaka, Y. Okada, S. Takeda, Nodal flow and the generation of left-right asymmetry. *Cell* **125**, 33–45 (2006).
10. P. Spéder, A. Petzoldt, M. Suzanne, S. Noselli, Strategies to establish left/right asymmetry in vertebrates and invertebrates. *Curr. Opin. Genet. Dev.* **17**, 351–358 (2007).
11. S. A. Holley *et al*., A conserved system for dorsal-ventral patterning in insects and vertebrates involving sog and chordin. *Nature* **376**, 249–253 (1995).
12. E. M. De Robertis, H. Kuroda, Dorsal-ventral patterning and neural induction in Xenopus embryos. *Annu. Rev. Cell Dev. Biol.* **20**, 285–308 (2004).
13. C. M. Mizutani, E. Bier, EvoD/Vo: The origins of BMP signalling in the neuroectoderm. *Nat. Rev. Genet.* **9**, 663–677 (2008).
14. J. McGrath, S. Somlo, S. Makova, X. Tian, M. Brueckner, Two populations of node monocilia initiate left-right asymmetry in the mouse. *Cell* **114**, 61–73 (2003).
15. Y. Okada, S. Takeda, Y. Tanaka, J. I. Belmonte, N. Hirokawa, Mechanism of nodal flow: A conserved symmetry breaking event in left-right axis determination. *Cell* **121**, 633–644 (2005).
16. A. G. Kramer-Zucker *et al*., Cilia-driven fluid flow in the zebrafish pronephros, brain and Kupffer's vesicle is required for normal organogenesis. *Development* **132**, 1907–1921 (2005).
17. D. P. Norris, Cilia, calcium and the basis of left-right asymmetry. *BMC Biol.* **10**, 102 (2012).
18. T. Hibino, Y. Ishii, M. Levin, A. Nishino, Ion flow regulates left-right asymmetry in sea urchin development. *Dev. Genes Evol.* **216**, 265–276 (2006).
19. S. M. Shimeld, M. Levin, Evidence for the regulation of left-right asymmetry in *Ciona intestinalis* by ion flux. *Dev. Dyn.* **235**, 1543–1553 (2006).
20. D. Takao *et al*., Asymmetric distribution of dynamic calcium signals in the node of mouse embryo during left-right axis formation. *Dev. Biol.* **376**, 23–30 (2013).
21. S. Yuan, L. Zhao, M. Brueckner, Z. Sun, Intraciliary calcium oscillations initiate vertebrate left-right asymmetry. *Curr. Biol.* **25**, 556–567 (2015).
22. K. Taniguchi *et al*., Chirality in planar cell shape contributes to left-right asymmetric epithelial morphogenesis. *Science* **333**, 339–341 (2011).
23. N. González-Morales *et al*., The atypical cadherin dachsous controls left-right asymmetry in *Drosophila*. *Dev. Cell* **33**, 675–689 (2015).
24. T. Juan *et al*., Myosin1D is an evolutionarily conserved regulator of animal left-right asymmetry. *Nat. Commun.* **9**, 1942 (2018).
25. M. Saydmohammed *et al*., Vertebrate myosin 1d regulates left-right organizer morphogenesis and laterality. *Nat. Commun.* **9**, 3381 (2018).
26. J. Gros, K. Feistel, C. Viebahn, M. Blum, C. J. Tabin, Cell movements at Hensen's node establish left/right asymmetric gene expression in the chick. *Science* **324**, 941–944 (2009).
27. K. Nishide, M. Mugitani, G. Kumano, H. Nishida, Neurula rotation determines left-right asymmetry in ascidian tadpole larvae. *Development* **139**, 1467–1475 (2012).
28. S. Yamada *et al*., Wavy movements of epidermis monocilia drive the neurula rotation that determines left-right asymmetry in ascidian embryos. *Dev. Biol.* **448**, 173–182 (2019).
29. R. Kuroda, B. Endo, M. Abe, M. Shimizu, Chiral blastomere arrangement dictates zygotic left-right asymmetry pathway in snails. *Nature* **462**, 790–794 (2009).
30. A. Davison *et al*., Formin is associated with left-right asymmetry in the pond snail and the frog. *Curr. Biol.* **26**, 654–660 (2016).
31. H. Nishida, T. Stach, Cell lineages and fate maps in tunicates: Conservation and modification. *Zool. Sci.* **31**, 645–652 (2014).
32. K. Kishi, T. A. Onuma, H. Nishida, Long-distance cell migration during larval development in the appendicularian, *Oikopleura dioica*. *Dev. Biol.* **395**, 299–306 (2014).
33. K. Kishi, M. Hayashi, T. A. Onuma, H. Nishida, Patterning and morphogenesis of the intricate but stereotyped oikoplastic epidermis of the appendicularian, *Oikopleura dioica*. *Dev. Biol.* **428**, 245–257 (2017).
34. H.-C. Seo *et al*., Miniature genome in the marine chordate *Oikopleura dioica*. *Science* **294**, 2506 (2001). Correction in: *Science* **295**, 45 (2002).
35. F. Denoeud *et al*., Plasticity of animal genome architecture unmasked by rapid evolution of a pelagic tunicate. *Science* **330**, 1381–1385 (2010).
36. J. Martí-Solans *et al*., Coelimination and survival in gene network evolution: Dismantling the RA-signaling in a chordate. *Mol. Biol. Evol.* **33**, 2401–2416 (2016).
37. W. Deng, S. Henriet, D. Chourrout, Prevalence of mutation-prone microhomology-mediated end joining in a chordate lacking the c-NHEJ DNA repair pathway. *Curr. Biol.* **28**, 3337–3341.e4 (2018).
38. Y. Mikhaleva, O. Kreneisz, L. C. Olsen, J. C. Glover, D. Chourrout, Modification of the larval swimming behavior in *Oikopleura dioica*, a chordate with a miniaturized central nervous system by dsRNA injection into fertilized eggs. *J. Exp. Zoolog. B Mol. Dev. Evol.* **324**, 114–127 (2015).
39. A. M. Søviknes, D. Chourrout, J. C. Glover, Development of the caudal nerve cord, motoneurons, and muscle innervation in the appendicularian urochordate *Oikopleura dioica*. *J. Comp. Neurol.* **503**, 224–243 (2007).
40. H. Nishida, N. Satoh, Cell lineage analysis in ascidian embryos by intracellular injection of a tracer enzyme. I. Up to the eight-cell stage. *Dev. Biol.* **99**, 382–394 (1983).
41. T. Hirano, H. Nishida, Developmental fates of larval tissues after metamorphosis in the ascidian, *Halocynthia roretzi*. II. Origin of endodermal tissues of the juvenile. *Dev. Genes Evol.* **210**, 55–63 (2000).
42. M. Koga *et al*., High cell-autonomy of the anterior endomesoderm viewed in blastomere fate shift during regulative development in the isolated right halves of four-cell stage *Xenopus* embryos. *Dev. Growth Differ.* **54**, 717–729 (2012).
43. C. Troedsson, P. Ganot, J. M. Bouquet, D. L. Aksnes, E. M. Thompson, Endostyle cell recruitment as a frame of reference for development and growth in the Urochordate *Oikopleura dioica*. *Biol. Bull.* **213**, 325–334 (2007).
44. G. Fredriksson, R. Olsson, The subchordal cells of *Oikopleura dioica* and *O. albicans* (Appendicularia, Chordata). *Acta Zool.* **72**, 251–256 (1991).
45. T. Stach, Ontogeny of the appendicularian *Oikopleura dioica* (Tunicata, Chordata) reveals characters similar to ascidian larvae with sessile adults. *Zoomorphology* **126**, 203–214 (2007).
46. M. Ohkura *et al*., Genetically encoded green fluorescent Ca^{2+} indicators with improved detectability for neuronal Ca^{2+} signals. *PLoS One* **7**, e51286 (2012).
47. Y. Mikhaleva, O. Tolstenkov, J. C. Glover, Gap junction-dependent coordination of intercellular calcium signalling in the developing appendicularian tunicate *Oikopleura dioica*. *Dev. Biol.* **450**, 9–22 (2019).
48. M. Yoshida, N. Sensui, T. Inoue, M. Morisawa, K. Mikoshiba, Role of two series of Ca^{2+} oscillations in activation of ascidian eggs. *Dev. Biol.* **203**, 122–133 (1998).
49. V. L. Nixon, A. McDougall, K. T. Jones, Ca^{2+} oscillations and the cell cycle at fertilisation of mammalian and ascidian eggs. *Biol. Cell* **92**, 187–196 (2000).
50. R. Dumollard, C. Sardet, Three different calcium wave pacemakers in ascidian eggs. *J. Cell Sci.* **114**, 2471–2481 (2001).
51. P. Ganot, J. M. Bouquet, T. Kallesøe, E. M. Thompson, The *Oikopleura* coenocyst, a unique chordate germ cell permitting rapid, extensive modulation of oocyte production. *Dev. Biol.* **302**, 591–600 (2007).
52. M. Matsuo, T. A. Onuma, T. Omotezako, H. Nishida, Protein phosphatase 2A is essential to maintain meiotic arrest, and to prevent Ca^{2+} burst at spawning and eventual parthenogenesis in the larvacean Oikopleura dioica. *Dev. Biol.*, S0012-1606(19)30059-4 (2019).
53. G. Danks *et al*., OikoBase: A genomics and developmental transcriptomics resource for the urochordate *Oikopleura dioica*. *Nucleic Acids Res.* **41**, D845–D853 (2013).

Downloaded at Palestinian Territory, occupied on December 7, 2021
www.manaraa.com

54. K. Wang, T. Omotezako, K. Kishi, H. Nishida, T. A. Onuma, Maternal and zygotic transcriptomes in the appendicularian, *Oikopleura dioica*: Novel protein-encoding genes, intra-species sequence variations, and trans-spliced RNA leader. *Dev. Genes Evol.* **225**, 149–159 (2015).
55. S. Bassham, J. H. Postlethwait, The evolutionary history of placodes: A molecular genetic investigation of the larvacean urochordate *Oikopleura dioica*. *Development* **132**, 4259–4272 (2005).
56. A. Stolfi *et al*., Guidelines for the nomenclature of genetic elements in tunicate genomes. *Genesis* **53**, 1–14 (2015).
57. C. Cañestro, S. Bassham, J. Postlethwait, Development of the central nervous system in the larvacean *Oikopleura dioica* and the evolution of the chordate brain. *Dev. Biol.* **285**, 298–315 (2005).
58. K. Waki, K. S. Imai, Y. Satou, Genetic pathways for differentiation of the peripheral nervous system in ascidians. *Nat. Commun.* **6**, 8719 (2015).
59. T. Omotezako, A. Nishino, T. A. Onuma, H. Nishida, RNA interference in the appendicularian *Oikopleura dioica* reveals the function of the *Brachyury* gene. *Dev. Genes Evol.* **223**, 261–267 (2013).
60. T. Nishikata, I. Mita-Miyazawa, T. Deno, K. Takamura, N. Satoh, Expression of epidermis-specific antigens during embryogenesis of the ascidian, *Halocynthia roretzi*. *Dev. Biol.* **121**, 408–416 (1987).
61. S. Darras, H. Nishida, The BMP/CHORDIN antagonism controls sensory pigment cell specification and differentiation in the ascidian embryo. *Dev. Biol.* **236**, 271–288 (2001).
62. T. Omotezako, T. A. Onuma, H. Nishida, DNA interference: DNA-induced gene silencing in the appendicularian *Oikopleura dioica*. *Proc. Biol. Sci.* **282**, 20150435 (2015).
63. W. B. Wood, Evidence from reversal of handedness in C. elegans embryos for early cell interactions determining cell fates. *Nature* **349**, 536–538 (1991).
64. S. Abdul-Wajid, H. Morales-Diaz, S. M. Khairallah, W. C. Smith, T-type calcium channel regulation of neural tube closure and EphrinA/EPHA expression. *Cell Rep.* **13**, 829–839 (2015).
65. T. Akahoshi, K. Hotta, K. Oka, Characterization of calcium transients during early embryogenesis in ascidians *Ciona robusta* (*Ciona intestinalis* type A) and *Ciona savignyi*. *Dev. Biol.* **431**, 205–214 (2017).
66. R. E. Dolmetsch, K. Xu, R. S. Lewis, Calcium oscillations increase the efficiency and specificity of gene expression. *Nature* **392**, 933–936 (1998).
67. T. A. Onuma, M. Matsuo, H. Nishida, Modified whole-mount in situ hybridisation and immunohistochemistry protocols without removal of the vitelline membrane in the appendicularian *Oikopleura dioica*. *Dev. Genes Evol.* **227**, 367–374 (2017).
68. Y. Tanimoto *et al*., Calcium dynamics regulating the timing of decision-making in *C. elegans*. *eLife* **6**, e21629 (2017).

Downloaded at Palestinian Territory, occupied on December 7, 2021

www.manaraa.com